

ON THE UTILISATION OF VORTICITY AND STRAIN DYNAMICS FOR IMPROVED ANALYSIS OF STIRRED PROCESSES

Yann Bouremel[†], Michael Yianneskis, Andrea Ducci

Experimental and Computational Laboratory for the Analysis of Turbulence (ECLAT),

Division of Engineering, King's College London, Strand WC2R 2LS, UK;

[†]yann.bouremel@kcl.ac.uk.

Abstract. The present work is aimed at the development of methodologies suitable for the characterisation and quantification of the strain dynamics occurring in vortical structures in stirred vessels. Due to the complexity of mixing reactor design, a fundamental flow, such as that associated with a vortex ring, has been selected to develop a procedure to gain improved understanding of mixing mechanisms by assessing the competitive actions of the strain rate tensor, \mathbf{S} , and vorticity vector, $\boldsymbol{\omega}$. This flow exhibits similarities with the trailing vortex structure around impeller blades and is employed as a paradigm to develop analytical approaches, which are then applied to the vortex structure produced around a Rushton impeller. The identification of stretching and compression regions of strain and the quantification of the relevant terms is discussed in the context of drop dispersion and with reference to previously reported observations.

Key words: Mixing, Strain, Energy Dissipation, Vortex Ring, Trailing Vortex.

1 INTRODUCTION

Mixing is of paramount importance in the chemical, petrochemical and pharmaceutical industries, as almost half of their production lines involve mixing in stirred vessels, but further optimisation of related processes is hampered by incomplete understanding of the fluid mechanics of mixing. Consequently further investigations are necessary to obtain a better understanding of the different mixing mechanisms taking place at different spatial length scales in order to optimise chemical processes and reactor design. In the present work an effort is made to improve understanding of the strain fields of vortical structures in stirred vessels and particularly the trailing vortices, in the context of drop dispersion. In the mixing of a drop/blob of fluid injected into the turbulent velocity field in a stirred vessel, the blob responds to the velocity field and deforms in response to the eddies that move within the field [1]. The response of the blob depends on the eddy size (l_e) and intensity. Encountering an eddy much larger than its own characteristic dimension ($l_e \gg l_b$), the blob is likely to be convected without much, if any, deformation. If $l_e = O(l_b)$, then the blob will be deformed. The kind of deformation encountered in this case should depend on the type of eddy structure encountered: e.g. if squeezed between two counter-rotating eddies as in between trailing vortices, the blob is most likely to be elongated. On the other hand, the action of two co-rotating eddies may break the blob into smaller globules. If $l_e \ll l_b$, the dispersion of the blob into many smaller ones is likely to occur, reaching eventually as the eddies become smaller, sizes of the order of the Kolmogorov scale and, under the action of diffusion, the Batchelor scale in due course. Of course, the deformation and break-up process described above is only indicative and is affected by interfacial tension and other parameters.

The methodologies presented in this paper can provide better understanding and quantification of deformation processes in stirred vessels, for example drop break-up of dispersed phases

that occurs primarily in the vicinity of the agitator. Shear forces and turbulent fluctuations affect drop break-up; in relation to the observations made earlier, if the initial drop size is large compared to the turbulent scales, viscous shear has a major effect until the drop is broken up into smaller sizes, and subsequently turbulent fluctuations become dominant and shear effects become negligible.

Earlier works, such as those of [2] and [3], have considered drop dispersion mechanisms in vessels stirred by pitched-blade and radial discharge impellers, respectively. Two different dispersion mechanisms were identified, both occurring in the trailing vortex system emanating from the impeller blades: these were termed ligament stretching and turbulent fragmentation. These mechanisms are reminiscent of the $l_e = O(l_b)$ and $l_e \ll l_b$ situations mentioned earlier; although present for both types of impeller, they exhibited differences, while blade thickness was found to influence ligament stretching.

Vortex dynamics and the quantification of the stretching/compression induced by vortical structures involves considerable complexity. For this reason, the relevant methodology is first developed on a comparatively simple flow, the vortex ring. The selection of this flow as a simple flow where the interaction of strain and rotation can be studied in detail was based on the observations of [4, 5, 6]. Such a flow exhibits similarities with the trailing vortices emanating from an impeller blade; it is however simpler and thus more amenable as a paradigm to help comprehend the far more complex trailing vortex flow.

2 FLOW CONFIGURATION AND EXPERIMENTAL APPARATUS

Particle Image Velocimetry (PIV) measurements were obtained to study the vorticity and strain dynamics of the vortex ring; for the trailing vortex study, the phase-resolved Laser Doppler Anemometry (LDA) measurements of [7] were employed to calculate the vortex dynamics of interest for the present work. In [7], a standard vessel of diameter $T=150$ mm stirred by a Rushton turbine of diameter $D_v = T/3$ and blade thickness $0.04D_v$ was used. The impeller clearance and speed were $T/3$ and $N=2670$ rpm ($Re = ND_v^2\nu^{-1} = 2780$), respectively, while the working fluid was white oil, FC 2012 W, of viscosity $\nu=4 \times 10^{-5}$ m²s⁻¹. The vortex ring flow was produced by a piston pushing a column of water inside a tube of diameter $D = 28.6$ mm which opened into an expansion chamber where the vortex ring was formed. A sketch of the experimental rig used is shown in figure 1.

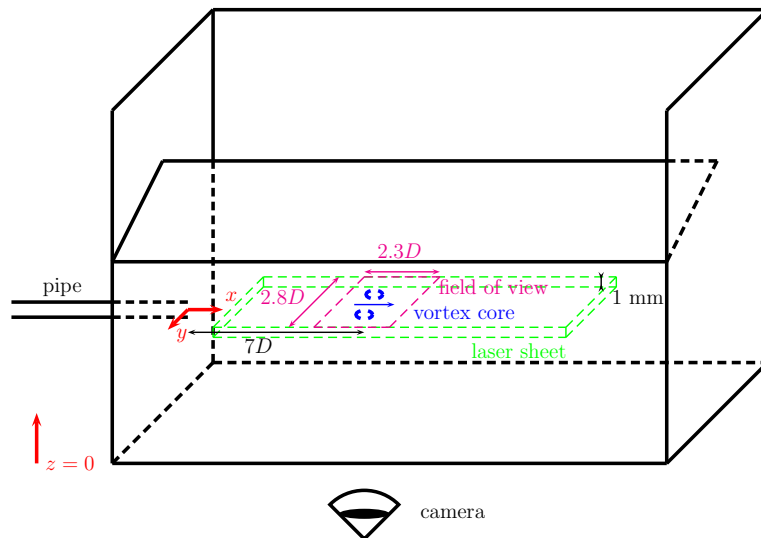


Fig. 1: Sketch of the experimental rig generating the vortex ring.

The experiments for the vortex strain dynamics presented in this paper were carried for $Re=4290$ ($Re=\frac{1}{2}LU_p\nu$) with the piston stroke being $L = 4D$; the piston velocity, $U_p = 7.5$ cm

s^{-1} and the viscosity of water, $\nu = 10^{-6} \text{ m}^2\text{s}^{-1}$. To prevent the formation of a trailing jet and piston vortices behind the vortex ring, the piston stroke was terminated inside the pipe at a distance of $1D$ from the tube exit. The flow field produced by the vortex ring was investigated at an axial distance centered around $x = 7D$ from the pipe exit, where the vortex is propagated forward by its self induced velocity [8, 9].

3 DEFORMATION RATE TENSOR

The stresses cause deformations of the fluid elements that are determined by the spatial variations of the velocities u_i : $\frac{\partial u_i}{\partial x_j}$ called the rate-of-deformation tensor. The fluid deformation $\frac{\partial u_i}{\partial x_j}$ is decomposed into a pure rate-of-deformation tensor, called the rate-of-strain tensor, and a pure rate-of-rotation tensor (see equation 1).

$$\frac{\partial u_i}{\partial x_j} = \frac{1}{2} \left(\frac{\partial u_i}{\partial x_j} + \frac{\partial u_j}{\partial x_i} \right) + \frac{1}{2} \left(\frac{\partial u_i}{\partial x_j} - \frac{\partial u_j}{\partial x_i} \right) = S_{ij} + \Omega_{ij} \quad (1)$$

with S_{ij} being the rate-of-strain tensor and Ω_{ij} being the rate-of-rotation tensor. The rate-of-deformation tensor $\frac{\partial u_i}{\partial x_j}$ can be decomposed along the principal axes of the \mathbf{S} tensor to visualise and quantify the main direction of stretching and compression [4].

$$\nabla \mathbf{u} = \begin{pmatrix} S_{11}^* & 0 & 0 \\ 0 & S_{22}^* & 0 \\ 0 & 0 & S_{33}^* \end{pmatrix} + \frac{1}{2} \begin{pmatrix} 0 & -\omega_3^* & \omega_2^* \\ \omega_3^* & 0 & -\omega_1^* \\ -\omega_2^* & \omega_1^* & 0 \end{pmatrix} \quad (2)$$

with S_{11}^* , S_{22}^* , S_{33}^* being the eigenvalues of \mathbf{S} and ω_1^* , ω_2^* , ω_3^* being the components of the vorticity along the principal axes of \mathbf{S} for each point. Each S_{ii}^* and the corresponding eigenvector define the local intensity and direction of stretching or compression; if $S_{ii}^* > 0$, the fluid element considered is stretched, whereas if $S_{ii}^* < 0$, the fluid is compressed.

Furthermore, according to this coordinate system, the energy dissipation ϵ can be expressed in terms of the stretching and compression eigenvalues (S_{ii}^*) as shown in equation 3 [4]:

$$\epsilon = 2\nu S_{ij} S_{ij} = 2\nu (S_{11}^{*2} + S_{22}^{*2} + S_{33}^{*2}) \quad (3)$$

4 VORTEX RING STRAIN DYNAMICS

As mentioned in section 2, the current investigation focuses on the laminar flow present around a vortex ring at a distance of $7D$ from the pipe exit, before transition of the vortex ring to the unstable-wavy and, eventually, turbulent regimes occurs. The vorticity and velocity vectors of the instantaneous cross-section of the vortex ring, for a stroke ratio of $L/D = 4$ and a piston velocity of $U_p = 7.5 \text{ cm/s}$, are shown in figure 2 where two vortex cores of opposite vorticity of equal magnitude ($\omega_{3_{max}} = \|\omega_{3_{min}}\| = 32U_p/L$) are present. It has to be stressed that the different contour plots shown in the rest of the section were obtained by averaging the instantaneous flow fields (similar to the one shown in figure 2) over an interrogation area of size $2.5D \times 2.46D$ moving with the vortex for 60 consecutive frames, recorded with a frequency of 235 Hz.

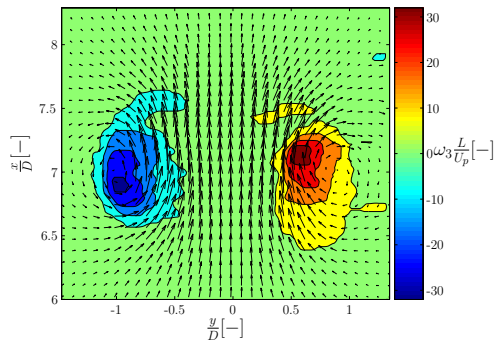


Fig. 2: Instantaneous vorticity contour and velocity vector plots of the vortex ring flow at $x/D = 7$.

The contour plots of the principal components of the strain rate tensor S_{11}^* , S_{22}^* and S_{33}^* are shown in figures 3 (a), (b) and 5, respectively. It should be noted that the translational velocity (U_{tr}) of the vortex ring was subtracted from the velocity fields before estimating the strain rate tensor, and that the component S_{33}^* associated to the fluid strain rate perpendicular to the plane of measurement was obtained from the continuity equation for an incompressible fluid (i.e. $\partial u_z/\partial z = -\partial u_x/\partial x - \partial u_y/\partial y$). A reference contour line delimiting the border of the vortex core is also shown in white in figures 3 (a), (b) and 5. A comparison between the contour plots of figures 3 (a) and (b) shows that the eigenvalues S_{11}^* and S_{22}^* assume solely positive and negative values, respectively, in the entire field of view, with the region in front of the vortex being mainly subject to compression, $-8 < S_{22}^* \frac{L}{U_p} < -5$, and the region behind the vortex being dominated by stretching, $3 < S_{11}^* \frac{L}{U_p} < 7$. The black contour lines reported in figures 3 (a) and (b) are tangent to the direction of the local eigenvectors associated to the eigenvalues S_{11}^* and S_{22}^* , respectively. Considering the front part of the vortex in figure 3 (b), the direction of compression is aligned with the vortex axis (x direction) for $y/D \approx 0$, indicating that still fluid ahead of the vortex ring is squeezed as the vortex ring gets closer. At the same time, fluid particles approaching the vortex ring are stretched in the direction perpendicular to the vortex axis by the two counter-rotating vortex cores. This behaviour is evident in figure 3 (a) where, for small values of y/D , the eigenvectors associated to S_{11}^* are directed as y . A sketch representing the combined effect of stretching and compression is shown in figure 4. At the rear of the vortex ring core, the direction of compression and stretching are inverted as fluid particles are squeezed in the direction perpendicular to the vortex ring translational velocity (U_{tr}) by the two coner-rotating vortex cores and stretched along the x axis as the vortex moves away.

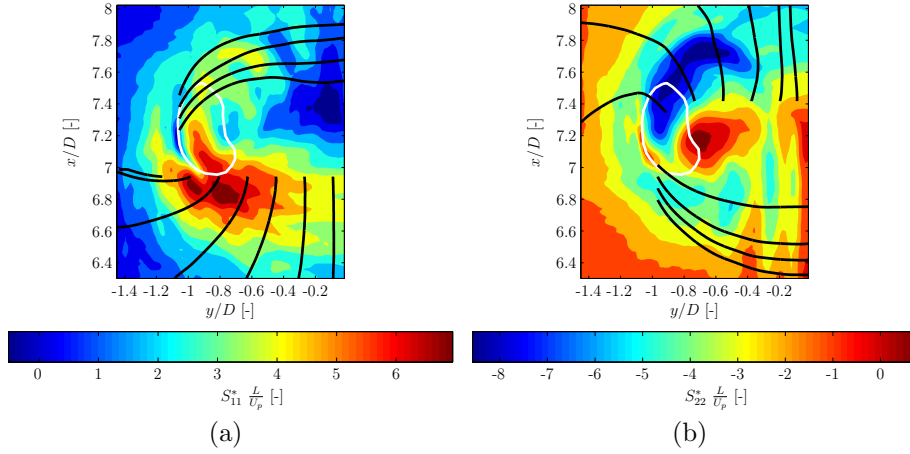


Fig. 3: Plots of the contour of the i_{th} eigenvalue S_{ii}^* and of selected reference contour lines locally tangent to the corresponding eigenvector: (a) S_{11}^* ; (b) S_{22}^* .

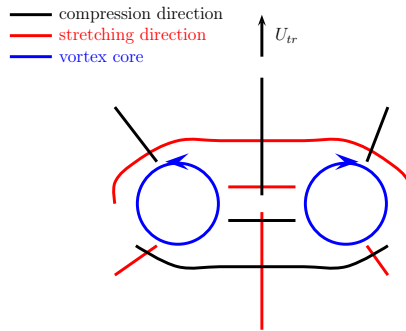


Fig. 4: 2D sketch of the compression and stretching directions at the front and rear of a vortex ring.

The contour plot of S_{33}^* is shown in figure 5. It should be stressed that the current experiments were 2 dimensional, and therefore the third component of the strain rate tensor was estimated by applying the continuity equation ($\partial u_z/\partial z = -\partial u_x/\partial x - \partial u_y/\partial y \Leftrightarrow S_{33}^* = -S_{11}^* - S_{22}^*$). The contours of S_{33}^* show opposite behaviour at the front and rear sides of the vortex with fluid particles approached by the vortex being stretched in the direction orthogonal to the measurement plane, $1.5 < S_{33}^* \frac{L}{U_p} < 3.5$, and fluid particles left behind the vortex being compressed with $-5 < S_{33}^* \frac{L}{U_p} < -2$. Considering the axis-symmetry in the x direction of the flow field investigated, this behaviour is expected, and the third eigenvalue S_{33}^* directed as z must display a similar trend to those eigenvalues that are directed as y at the front and rear part of the vortex. In other words the front (rear) side of the vortex is subject to bi-axial stretching (bi-axial compression) along the two directions perpendicular to the vortex axis associated to the eigenvalues S_{11}^* (S_{22}^*) and S_{33}^* with local stretching rates (compression rates) of comparable magnitude.

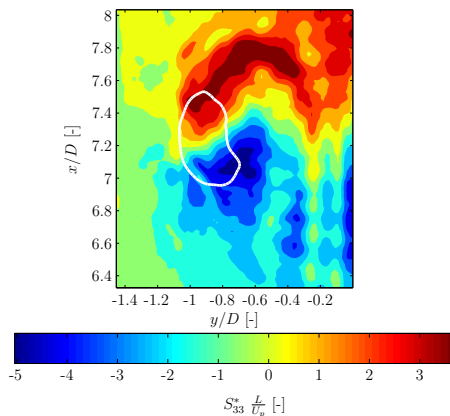


Fig. 5: Contour plot of the strain rate S_{33}^* directed orthogonally to the measurement plane.

The local energy dissipation rate distribution, obtained from equation (3), was also calculated (not shown here for brevity of presentation). As expected the non-dimensional dissipation rate ($\frac{\epsilon L}{U_p^3}$) assumed peak values at the border of the vortex core ($2 - 2.5 \times 10^{-6}$) where the local strain and compression rates reach their absolute maxima.

5 TRAILING VORTEX STRAIN DYNAMICS

The methodology described earlier is applied in this section to the flow field of the trailing vortices in the impeller stream region of a vessel stirred by a Rushton turbine. The phase-resolved LDA velocity data of [7] were employed for this purpose. The current investigation of the strain dynamics occurring in the trailing vortex region has focused to a phase angle of $\phi = 15^\circ$ behind the blade when the local energy dissipation rate is maximum [10] and therefore local strain rates should be more significant. A cylindrical coordinate system is considered with its axis aligned with the vessel one and its origin set at the bottom of the vessel. The plots of the vorticity contour and velocity field associated to the trailing vortices for $\phi = 15^\circ$ are shown in figure 6. It should be noted that in figures 6, 7 and 8 the impeller is rotating clockwise as seen from above and therefore the blade shown at the right of the impeller axis is approaching the vertical plane of measurement, while the blade pictured at the left of the axis (only in figures 7 and 8) is leaving the plane of measurement. The two counter-rotating trailing vortices, positioned at $r/D_v \approx 0.5$, are only approximately symmetric with respect to the radial direction, with local absolute vorticity maxima of $\|\omega_3(\pi N)^{-1}\| = 18$.

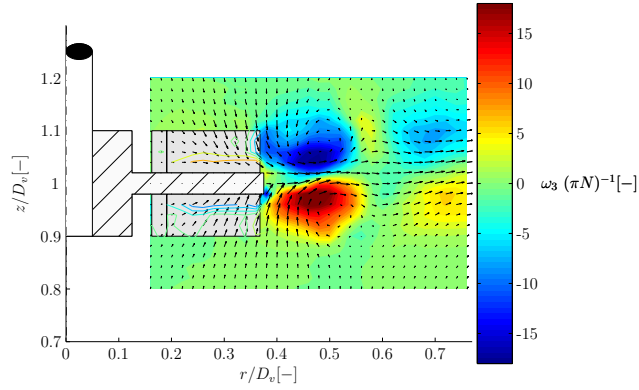


Fig. 6: Vorticity contour and velocity vector plots of the trailing vortices for $\phi = 15^\circ$

The contour plots of the non-dimensional strain rates, $S_{11}^*(\pi N)^{-1}$ and $S_{22}^*(\pi N)^{-1}$ are shown in the right hand side (RHS) of figures 7 and 8, respectively. Similarly to the discussion already made for the vortex ring flow, regions dominated by stretching and compression are present in the front and the back parts of the trailing vortices with $S_{11}^*(\pi N)^{-1}$ values of approximately 6 and -2, respectively (see figure 7). It should be noted however that the trailing vortex flow is far more complex than the one associated to vortex rings, and the nearly radial jet coming out of the impeller blade results in higher strain rates (i.e. $S_{11}^*(\pi N)^{-1}$ up to 7.5) along the impeller stream centreline in the proximity of the disk. A clearer picture of the strain dynamics can be obtained by considering the left hand side (LHS) of figure 7, where reference contour lines tangent to the local strain rate directions are plotted with hues varying according to the local magnitude of $S_{11}^*(\pi N)^{-1}$. As expected for axial positions close to the impeller centerline, the strain rate S_{11}^* is positive and almost horizontal, indicating that the impeller jet is responsible for the local high strain region.

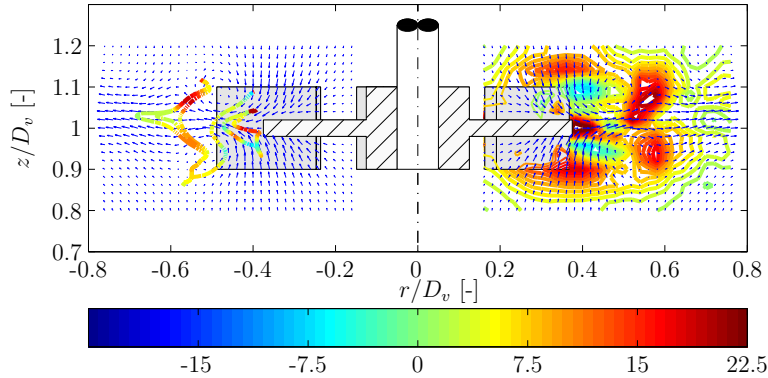


Fig. 7: Contour plot of the non-dimensional eigenvalue $S_{11}^*(\pi N)^{-1}$ (RHS) and plot of contour lines locally tangent to the direction of S_{11}^* (LHS).

The contour plot of S_{22}^* with the corresponding contour lines tangent to the local strain rate directions are shown in the RHS and LHS of figure 8, respectively. S_{22}^* is mainly negative, and in agreement with the vortex ring strain dynamics shown in the sketch of figure 4, the compression lines in the front part of the vortex are nearly orthogonal to the local vortex velocities. It should be noted however that the maximum compression rate is registered in proximity of the impeller disk, where the streams of fluid sucked in the impeller region from the upper and lower part of the vessel merge together. Along the centreline S_{22}^* is directed vertically as fluid particles that are stretched by the impeller jet in the radial direction are simultaneously compressed in the vertical one.

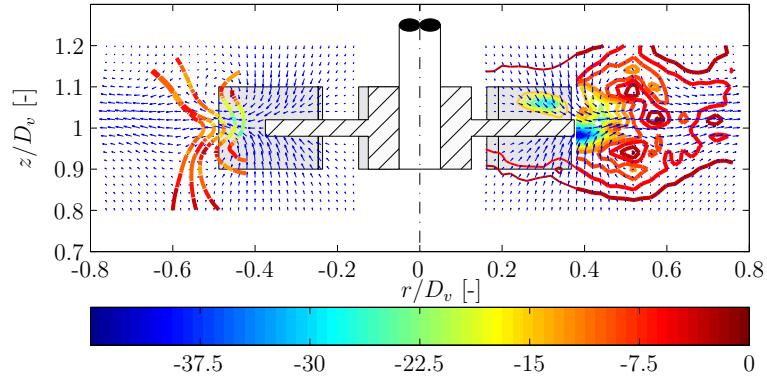


Fig. 8: Contour plot of the non-dimensional eigenvalue $S_{22}^*(\pi N)^{-1}$ (RHS) and plot of contour lines locally tangent to the direction of S_{22}^* (LHS).

The data presented above can be employed to calculate the total viscous stress at any point in the vortex region from equation (4), where repeated indices indicate summation:

$$\|\sigma\| = 2\eta\sqrt{S_{ii}^{*2}} \quad (4)$$

Such results can then be juxtaposed with estimations taking into account the interfacial tension, initial drop/blob size and other parameters and properties of dispersions to aid understanding of drop deformation and bursting which are promoted primarily by the straining motion in the shear present in the flow [11]. Indeed, estimates of strain magnitudes based on the data presented above together with interfacial tension considerations are in agreement with the trends exhibited by the experiments of [3] with initial and final drop sizes of around 30 mm (20-40 mm) and 2 mm respectively. The results show promise for the improved understanding and prediction of drop deformation and mixing processes, but further research is necessary over a wider range of stirred vessel parameters.

6 CONCLUDING REMARKS

The vorticity and strain dynamics have been studied in an effort to develop approaches suitable for the improved understanding and calculation of the deformation and break-up mechanisms taking place in stirred vessels. The procedure was developed in a vortex ring flow and subsequently applied to the trailing vortex structure around a Rushton impeller. Regions of stretching and compression of the flowfields studied were identified and the approach shows promise for the more detailed characterisation and further optimisation of stirred processes.

ACKNOWLEDGEMENTS

Financial support for the work reported here was provided by the Engineering and Physical Sciences Research Council (EPSRC) of the UK, grant EP/D032539. The authors gratefully acknowledge provision of the stirred vessel LDA velocity data by Dr. Marcus Schäfer [7] acquired as part of the BRITE-EURAM project BRPR-CT96-0185.

NOMENCLATURE

S_{ii}^* : Rate-of-strain along the i^{th} principal axis [s^{-1}]	S_{ij} : Rate-of-strain tensor [s^{-1}]
ω_i^* : Vorticity in the i^{th} principal direction of S [s^{-1}]	ω_i : Vorticity in the i^{th} direction [s^{-1}]
l_e : Eddy size [m]	l_b : Blob size [m]
Ω_{ij} : Rate-of-rotation tensor [s^{-1}]	ϵ : Energy dissipation [m^2/s^3]
σ : Viscous stress tensor [N/m^2]	U_p : Piston velocity [m/s]

References

1. S. M. Kresta, R. S. Brodkey, Turbulence in mixing applications, in: E. L. Paul, V. A. Atiemo-Obeng, S. M. Kresta (Eds.), Handbook of Industrial Mixing: Science and Practice, John Wiley & Sons, New Jersey, 2004, pp. 43–45.
2. A. M. Ali, H. H. S. Yuan, D. S. Dickey, G. B. Tatterson, Liquid dispersion mechanisms in agitated tanks: Part I. Pitched blade turbine., Chem. Eng. Commun. 10 (1981) 205–213.
3. T. P. K. Chang, Y. H. E. Sheu, G. B. Tatterson, D. S. Dickey, Liquid dispersion mechanisms in agitated tanks: Part II. Straight blade and disc style turbines., Chem. Eng. Commun. 10 (1981) 215–222.
4. P. A. Davidson, Turbulence an introduction for scientists and engineers, Oxford University Press, 2004.
5. K. B. Southerland, J. R. Porter III, W. J. A. Dahm, K. A. Buch, An experimental study of the molecular mixing process in an axisymmetric laminar vortex ring, Phys. Fluids 5 (1991) 1385–1392.
6. P. Meunier, E. Villermaux, How vortices mix, J. Fluid Mech. 476 (2003) 213–222.
7. M. Schäfer, Charakterisierung, auslegung und verbesserung des makro- und mikromischens in gerührten behältern, Ph.D. thesis, Der Technischen Fakultät der Universität Erlangen-Nürnberg, Germany (2001).
8. K. Shariff, A. Leonard, Vortex rings, Annu. Rev. Fluid Mech. 24 (1992) 235–272.
9. M. Rosenfeld, E. Rambod, M. Gharib, Circulation and formation number of laminar vortex rings, J. Fluid Mech. 376 (1998) 297–318.
10. A. Ducci, M. Yianneskis, Direct determination of energy dissipation in stirred vessels with two-point LDA, AIChE J. 51 (8) (2005) 2133–2148.
11. J. M. Rallison, The deformation of small viscous drops and bubbles in shear flows., Annu. Rev. Fluid Mech. 16 (1984) 45–66.